VOL. 21, NO. 10, MAY 2026 ISSN 1819-6608
ARPN Journal of Engineering and Applied Sciences
©2006-2026 Asian Research Publishing Network (ARPN). All rights reserved.
www.arpnjournals.com

HYBRID PV-BATTERY-SUPERCAPACITOR SYSTEM FOR ENHANCED GRID STABILITY AND COST EFFICIENCY: A MULTI-OBJECTIVE OPTIMIZATION APPROACH

Kevin Sonon[1], Patrice Chetangny[1], Mèhundo Walix Leslie D. E.[1], Victor Zogbochi[1], Sossou Houndedako[1], Didier Chamagne[2] and Gérald Barbier[3]
[1]Laboratoire d'Electrotechnique, de Télécommunication et d'Informatique Appliquée (LETIA), Université d'Abomey-Calavi (UAC), Bénin
[2]Université Marie et Louis Pasteur, CNRS, Institut FEMTO-ST, F-90000 BELFORT, France
[3]Laboratoire de Physique et Mécanique Textiles (LPMT) Université de Haute Alscase (UHA - ENSIA) Mulhouse, France
E-Mail: elisee.sonon@gmail.com

ABSTRACT

The integration of renewable energies, particularly photovoltaics (PV), into electrical grids presents significant challenges in terms of stability and intermittency management. This article introduces an innovative hybrid system that combines a 25 MWc PV plant, lithium-ion batteries, and supercapacitors, connected to the grid via a 161 kV interface. The main objective is to achieve a balance between energy performance, grid stability, and economic profitability. Detailed component modeling is performed using Simulink, while PowerFactory is employed for grid-scale stability analysis. The multi-objective optimization of storage capacities is conducted using the NSGA-II algorithm, aiming to minimize both the total cost and the amount of imported energy. The system provides rapid response to load peaks through supercapacitors, while the batteries cover the medium-term energy needs. Simulations confirm stable grid operation under disturbances, with voltage and frequency maintained within acceptable ranges. The validation using PowerFactory and real-world testing at the DEFISOL site further confirms the robustness of the proposed model. Despite certain simplifying assumptions, this study marks a significant step toward more resilient and sustainable electrical networks in the context of the ongoing energy transition.

Keywords: photovoltaic system, lithium-ion battery, supercapacitor, hybridization, grid stability, NSGA-II optimization.

Manuscript Received 12 April 2026; Revised 30 April 2026; Published 20 July 2026

1. INTRODUCTION

The energy transition towards renewable sources is a global priority to reduce greenhouse gas emissions and ensure sustainable electricity production [1]. Among these sources, photovoltaic (PV) energy occupies a central place due to its abundance, modularity, and ease of integration into electrical grids [2]. A good estimation of solar potential is a prerequisite for any sizing approach [3]. In this context, we have developed a method for analyzing climatic data that allows for a reliable assessment of solar and wind potential [4]. However, PV production is subject to significant variability due to weather conditions (irradiation, temperature), which leads to intermittency that can destabilize electrical grids [5]. To mitigate these effects, the hybridization of PV systems with energy storage solutions, combined with a grid connection, constitutes a promising strategy [6]. Lithium-ion batteries, thanks to their high energy density and longevity, are well-suited for medium-term storage, while supercapacitors, characterized by their high specific power and rapid response time, effectively manage rapid load fluctuations [7] [8]. This complementarity between technologies allows for the absorption of excess PV production and compensates for deficits during peak demand [9] [10], thereby improving grid stability and increasing the penetration rate of renewable energy.

However, several technical challenges remain. The dynamic management of intermittencies requires advanced regulation mechanisms to maintain the balance between production and consumption [11].

The optimal sizing of storage capacities, including batteries and supercapacitors, must take into account costs, component lifespan, and technical constraints of the grid [12][13].

Moreover, the injection of intermittent energy can cause voltage and frequency variations that may compromise the quality of the distributed electricity [14].

Recent studies have shown that the integration of advanced control strategies, such as MPPT algorithms and active storage management, combined with multi-objective optimization via NSGA-II, can significantly improve the efficiency of hybrid systems [15] [16]. Nevertheless, few studies jointly address the detailed modeling of components (PV, batteries, supercapacitors and the analysis of their impact on large-scale grid stability.

It is in this context that the present work is situated, which is distinguished by the unprecedented coupling of three complementary tools: Simulink for the dynamic modeling of components, PowerFactory for network stability analysis (voltages, frequencies, fault currents), and NSGA-II for the multi-objective optimization of storage capacities, reconciling energy

©2006-2026 Asian Research Publishing Network (ARPN). All rights reserved.

performance, network stability, and economic profitability. Unlike existing studies, often limited to partial simulations or local scales, this integrated approach allows for a holistic and realistic evaluation of a system. A hybrid PV-storage system is connected to the grid.

2. MATERIALS AND METHODS

A. Modeling of the Hybrid System

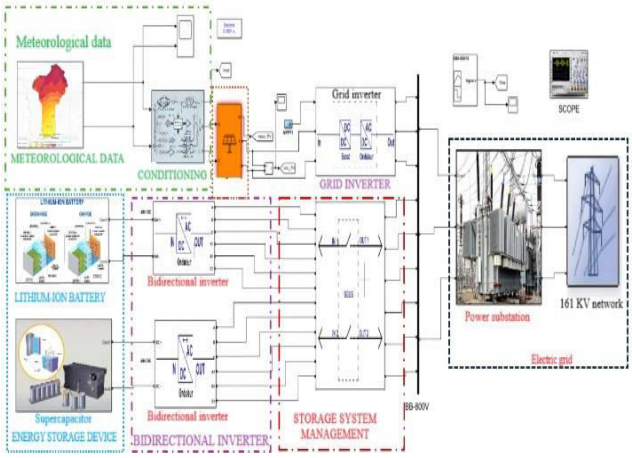


Figure-1. Simulink model of the entire photovoltaic system.

a) Global Architecture

The hybrid system we propose is based on an integrated architecture combining three major components (Figure-1). The 25 MWc photovoltaic power plant, consisting of Jinko Solar TR72M 530W modules, forms the main source of renewable energy. It is coupled with an innovative hybrid storage system, including lithium-ion batteries for medium-term energy storage and supercapacitors for response to rapid transients.

The entire system is connected to the electrical grid via a 161 kV interface, allowing both energy injection and grid stabilization. The Simulink module is based on a five-parameter model to describe the current-voltage characteristics, including a current source induced by insolation, a diode, a series resistance, and a parallel resistance.

The key elements of the module include the maximum power, which is the highest power obtained, the open-circuit voltage, which is the voltage when the circuit is open, and the short-circuit current, which is the current in a short-circuit situation.

This model takes into account:

- The dependence on irradiation and temperature
- Losses due to mismatch effect
- The non-linear I-V characteristics

The voltage at the maximum power point, denoted, corresponds to the voltage at which the power delivered by the solar panel is maximum. Similarly, the current at the maximum power point, denoted, is the current for which the power is maximum. The temperature coefficient of open-circuit voltage represents the variation of the open-circuit voltage as a function of temperature.

The five-parameter model presented in Figure-2 describes the relationship between current and voltage in a photovoltaic cell. It also takes into account the impact of temperature and solar irradiation on the power delivered by the panel.

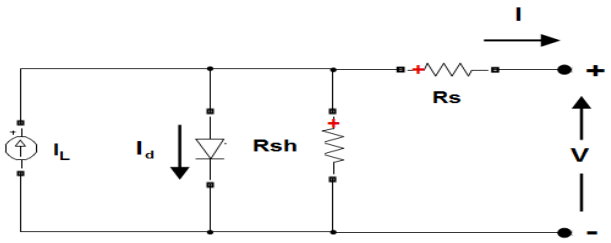


Figure-2. Five-parameter model used by the PV field block in Simulink.

The electrical behavior of the modules is described by the 5-parameter characteristic in (1).

$$I = I_L - I_O\left[\exp\left(\frac{V + IR_S}{a}\right) - 1\right] - \frac{V + IR_S}{R_{sh}} \quad (1)$$

The adopted configuration includes 29 modules in series per string and 1626 strings in parallel, allowing the nominal voltage of 1181.46 V to be reached at the inverter input. The inverter used is composed of two essential stages (Figure-3). We first have a Boost converter (DC-DC), followed by a DC-AC converter (the inverter itself).

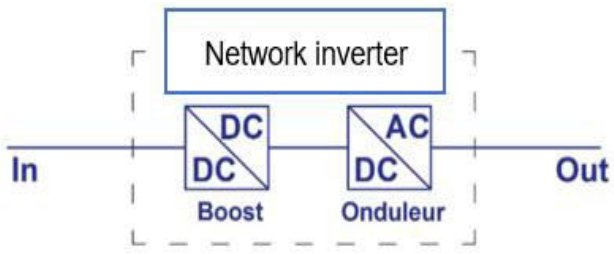


Figure-3. Equivalent of the grid inverter modeled in Simulink.

The representation in Simulink with the blocks illustrating each stage of the inverter is presented in Figure-4.

©2006-2026 Asian Research Publishing Network (ARPN). All rights reserved.

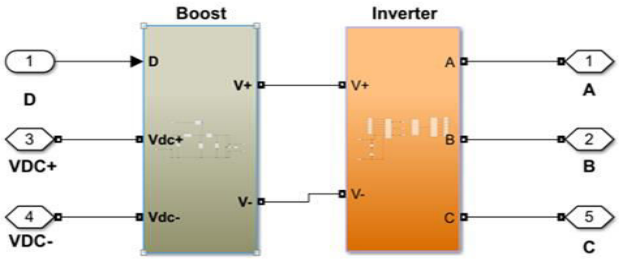


Figure-4. Network inverter.

The BOOST DC-DC converter (Figure-5), also called a Boost chopper, is a static converter that receives a DC voltage source at the input and provides an output signal that is also DC, but with a higher voltage.

The output voltage is proportionally higher than the input voltage.

In this work, the input voltage of the DC-DC stage reaches a maximum value of 1181.46 V, as the MPP voltage of a panel in the string is 40.74 V and a string consists of 29 photovoltaic modules in series. The output voltage of the BOOST converter was set to 1500 V to remain consistent with the maximum input value of the string inverters used at the DEFISOL site. The adopted MPPT control is based on the P&O (Perturb and Observe) method to generate the control signal for the electronic switch (IGBT) at the point of maximum power. The nominal duty cycle is thus 0.21.

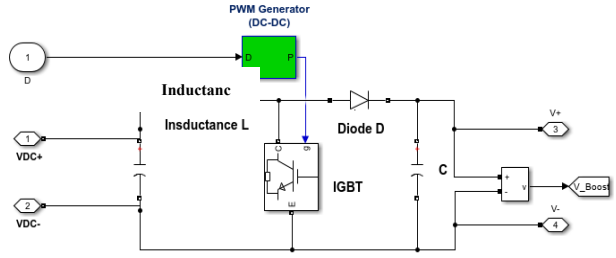


Figure-5. Simulink model of the BOOST converter DC-DC.

The values of the inductance and the capacitor are given by the following relations (2) and (3):

$$L > (\alpha.(1-\alpha)^2.V_e.R_s.T_c)/2 \quad (2)$$

$$C = \alpha.V_s.T_c./(R_s.\Delta V) \quad (3)$$

With:

V_s: the output voltage (1500V);
V_e: the input voltage (1181.46V);
α: the cyclic ratio, here equal to 0.21;
R_s: the output resistance of the DC-DC stage;
T_c: the period of the chopping signal.

The Simulink model of the BOOST DC-DC converter consists of an input capacitor with a certain capacitance, an inductor coil, an IGBT controlled by an input signal, a diode, and two output capacitors, each with a certain capacitance.

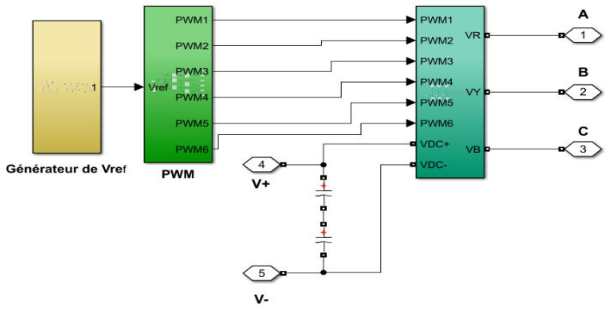


Figure-6. Constitutive sub-block of the DC-AC stage of the grid inverter.

The control signal for the IGBT is provided by a PWM generator at the switching frequency. The generator takes as input the duty cycle of the boost converter, which is controlled with an MPPT regulator following the P&O algorithm.

The second stage of the grid inverter is a DC-AC converter: a three-phase inverter.

Figure-6 shows the combination of the different blocks that make up the DC-AC stage of the grid inverter. Thus, we have:

- The input capacitors that filter the signal coming from the BOOST at the input;
- The 3-level IGBT transistor bridge that generates the three-phase wave signal to connect to the grid (Figure-7);
- The system for regulating and generating control signals for switching.

The parameters of the IGBT block are:

- The internal resistance Ron of the IGBT: it is measured in ohms (Ω), with a default value of;
- The damping resistance R_s: it is the resistance of the damping circuit, measured in ohms (Ω), with a default value of;
- By setting the R_s parameter to infinity (∞), the damper is eliminated from the model. The damping capacitance Cs is the damping capacitance measured in farads (F), with a default value of infinity.
- By setting the C_s parameter to 0, the snubber is eliminated, or to infinity to obtain a resistive snubber.

©2006-2026 Asian Research Publishing Network (ARPN). All rights reserved.

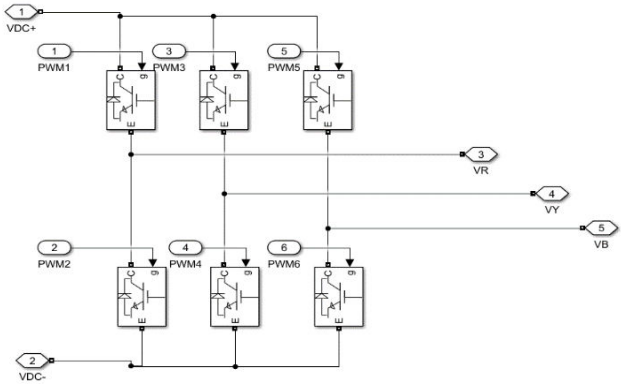


Figure-7. 3-level IGBT transistor bridge for the grid inverter.

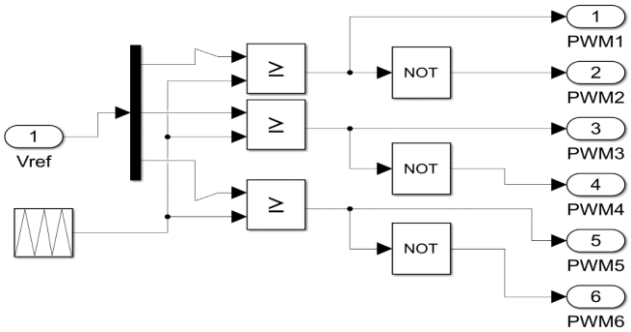


Figure-8. PWM signal to control the IGBTs of the Inverter Bridge.

Figure-8 shows the PWM signal driving the inverter's IGBTs.

The PWM, or modulating signal, is generated by comparing a reference signal (V_{ref}) of three components (three-phase signal) to a triangular signal, which is the carrier.

We have six complementary PWM signals in pairs so that the two transistors in the same arm never close at the same time to avoid a short circuit.

The V_{ref} voltage is obtained through the regulation block that integrates the phase-locked loop (PLL) control, which compares the measured frequency and phase with those of the inverter. If a difference is detected, the system adjusts the frequency and phase of the inverter to align them with those of the grid. Figure-9 presents the Simulink model of the process for generating the V_{ref} voltage, which served as the modulator to produce the PWM signal.

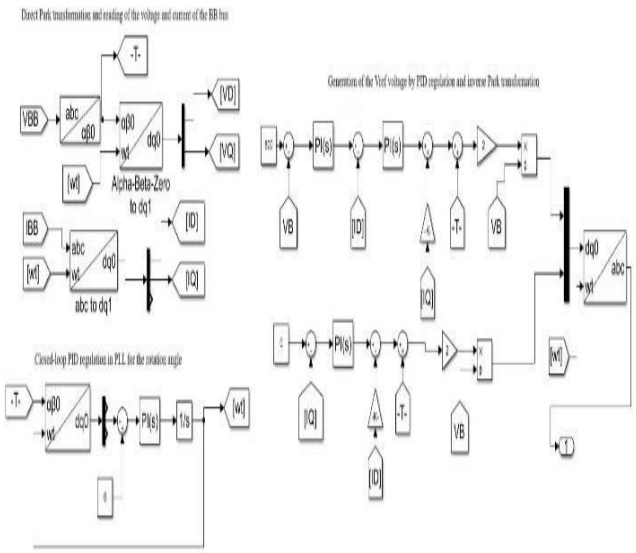


Figure-9. Modeling in Simulink of the V_{ref} voltage with PLL regulation of the rotation angle.

b) Hybrid Storage System

The storage system wisely combines two complementary technologies. The lithium-ion batteries, with a capacity of 281250 Ah, are modeled with particular attention to their internal resistance and state of charge (SOC).

Their relatively slow dynamics (time constant on the order of several minutes) contrast with those of supercapacitors, which can respond to sudden power variations in less than a second. The energy capacity of the pack can be expressed in terms of the depth of discharge and the total energy to be provided E_{tot} as in (4), (5), and (6).

$$SOC_{BAT} = SOC_{BAT_min} - \frac{1}{E_{BAT_max}} \int P_{BAT} \cdot dt \quad (4)$$

$$\Delta SOC_{BAT} = \frac{\Delta E_{BAT}}{E_{BAT_max}} \quad (5)$$

$$E_{BAT_max} = \frac{E_{tot}}{DOD_{BAT}} \quad (6)$$

The "Supercapacitor" block in Simulink uses an electrical model to simulate the behavior of the supercapacitor. It combines an ideal capacitance with an internal resistance (ESR).

The ideal capacity indicates the amount of energy that can be stored, while the internal resistance represents energy losses.

The charge and the discharge:

The block manages the charge and discharge based on the current passing through it. The voltage across

©2006-2026 Asian Research Publishing Network (ARPN). All rights reserved.

the terminals varies according to the amount of charge and the current, which can be expressed as in (7):

$$Q = C.V \quad (7)$$

Where:
Q: is the charge C: the capacitance and V: the voltage.
Charge and discharge current:

The block also takes into account the charge and discharge currents, thus modifying the voltage of the supercapacitor. A positive current means a discharge, and a negative current indicates a charge.

In Simulink, this block can be integrated with other electrical components in Simscape Electrical to simulate a circuit. It is particularly useful for analyzing the influence of the supercapacitor's characteristics on the performance of a system, such as an inverter, a DC-DC converter, or an energy storage system. This block was used in this work to simulate the storage system with supercapacitor.

The modeling of supercapacitors incorporates their main characteristic: the ability to deliver high power for short durations. Their sizing is based on a trade-off between the energy to be stored and the operating voltage, as shown by the fundamental equation describing the stored energy.

c) Converter and Control Strategy

The power interface is a crucial element of the system. The grid inverter, designed according to the IEC 62109 standard, includes two conversion stages: a boost converter to adapt the PV voltage to 1500 V DC, followed by a three-level three-phase inverter.

The latter incorporates a sophisticated PLL (Phase-Locked Loop) control to ensure perfect synchronization with the network. Bidirectional converters, on the other hand, allow for flexible energy exchanges between the grid and storage systems.

Their design underwent meticulous sizing, resulting in optimal duty cycles of 0.042 in Buck mode and 0.968 in Boost mode, with a switching frequency of 5 kHz to limit switching losses.

The sizing strategy used here is based on defining the storage capacity of supercapacitors in addition to batteries, taking into account the cutoff frequency of the first filter. In this context, the batteries provide the primary compensation for load fluctuations on the grid. However, when the demand exceeds a certain threshold, sudden power fluctuations can occur, requiring immediate compensation.

These variations, often comparable to power steps (Figure-10), result from the sudden commissioning of significant loads. In this case, the supercapacitors intervene by quickly providing the necessary energy, thus stabilizing the grid before the batteries gradually take over for more sustainable compensation.

In the case where supercapacitors are considered capable of powering frequency components on the order of 0.01 Hz, the associated time constant is 16 seconds. The maximum power to be covered by the supercapacitors is estimated at 1 MW.

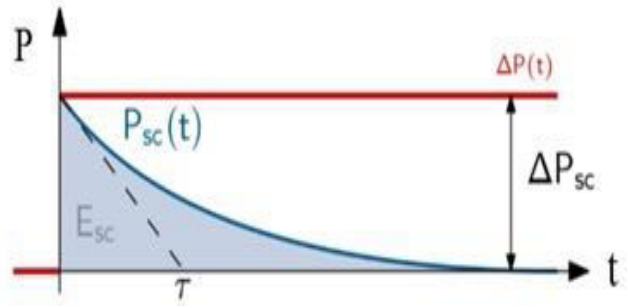


Figure-10. Step profile of the load.

We therefore assume the possible appearance of a step of this magnitude.

From this data, it is possible to determine the energy parameters necessary for sizing the supercapacitor bank, particularly the minimum and maximum power to be supplied. Taking into account a discharge depth of 90%, the energy stored by the supercapacitors is approximately 3600 MJ.

This leads to the selection of a 3,125 MF / 48 V supercapacitor bank, composed of BCAP0310 elementary modules from Maxwell. Each module has a nominal capacity of 310 F and a nominal voltage of 2.7 V.

The usable energy by each SC module is given by equations (8) and (9):

$$E_{sc} = \frac{1}{2} C_{sc} \left(V_{max}^2 - V_{min}^2 \right) \quad (8)$$

Avec:

$$V_{min} = 0.3 V_{max} \quad (9)$$

The SC bench consists of a number of modules calculated as follows (10):

$$N_{mod} = \frac{E_{sc}}{E_{mod_sc}} \quad (10)$$

Thus, the SC bench used is made up of 3266550 cells.

It is composed of 18 modules that are connected in series and 181475 branches in parallel. The characteristics of the supercapacitor bank used are summarized in the following Table-1.

©2006-2026 Asian Research Publishing Network (ARPN). All rights reserved.

Table-1. Characteristics of the supercapacitor bank.

Characteristics of the SC bench	
Number of cells (310F/2.7V)	**3266550**
Number of modules in series	18
Number of branches in parallel	181475
Nominal voltage	48V

d) Energy Management System

The switching block (Figure-11) or the Energy Storage Unit Management System (ESUMS) is responsible for managing the switching between charge and discharge modes of batteries and supercapacitors.

It thus manages the transition from the Battery Park to supercapacitors in case of a peak on the network.

Figure-11 shows the block diagram of the storage unit management system. Indeed, it is the module responsible for managing the energy flow between the grid (AC BUS) and the storage units via the bidirectional charger inverters of each storage station (Batteries and Supercapacitors).

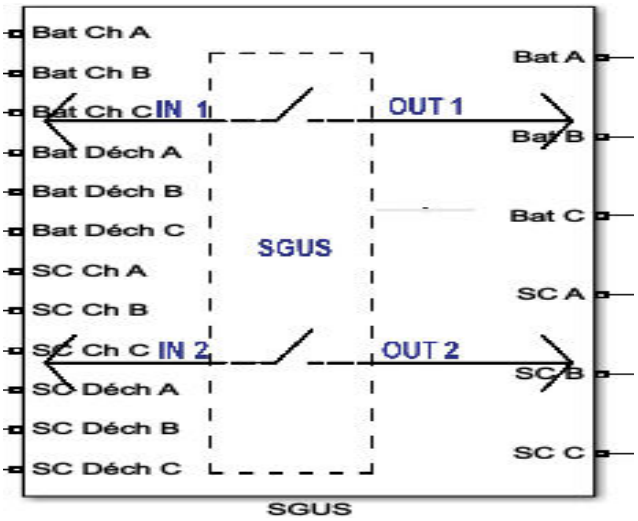


Figure-11. Block Storage Unit Management System (SGUS) implemented in Simulink.

The block is therefore used to control the charging or discharging of the batteries or supercapacitors according to well-defined and modeled conditions.

The Storage Unit Management System (SUMS) represents the brain of the installation. Its decision-making algorithm relies on real-time multi-criteria analysis, taking into account:

For the batteries:

- The batteries switch to charging mode when the SOC is below 100% and the irradiation is above 300 W/m², that is, from the start of solar production;
- They switch to discharge mode during the night time peak period between 6 PM and 10 PM and when the SOC is above 70%.

For supercapacitors:

- The supercapacitors switch to charging mode when the SOC is below 100%, and the active power of the load (consumption profile) is less than or equal to the threshold of 12.5 MW:
- The supercapacitors discharge only when the load on the grid (Vload_ref) exceeds the threshold value of 12.5 MW and the SOC is above 70%.

This strategy allows for optimal management of energy flows, ensuring both the lifespan of storage equipment and the stability of the network.

Figure-12 presents the details of the Simulink block of the Storage Unit Management System.

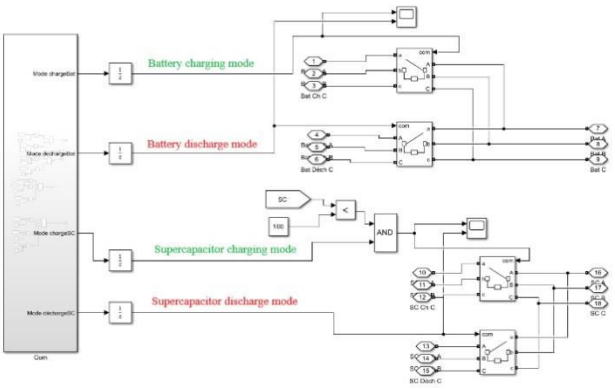


Figure-12. Detailed block diagram of the Storage Unit Management System in Simulink.

- The Planning criteria adopted to ensure the proper functioning of the network in a static regime in a healthy state (Availability of all network structures) are:
- Voltage at the nodes High Voltage, (HV): ± 5% of the nominal voltage;
- Load of an HT structure (line or transformer), < 100% of its nominal capacity;
- Reactive power of the production units within the permissible margin;
- The criteria adopted to ensure the proper functioning in static regime of the transport network in disturbed state for the N-1 security criterion (Unavailability of a network facility) are:
- Voltage at the nodes High Voltage (HV): ± 10% of the nominal voltage;
- Load of an HT line, that is <110% of its nominal capacity;
- Load of a high voltage transformer, i.e., <120% of its nominal capacity;
- Reactive power of production units within the permissible margin.

©2006-2026 Asian Research Publishing Network (ARPN). All rights reserved.

For the dynamic stability study conducted as part of this work, in order to evaluate the impact of short-circuit currents from storage devices as well as the photovoltaic power plant, the values of short-circuit currents in the high-voltage substations of the electricity transmission network, calculated according to the IEC 60909 standard in a healthy state, must not exceed the permissible values corresponding to the breaking capacities of the circuit breakers. Namely:

- 330 kV: 50 kA; - 161 kV: 40 kA.

The time for eliminating three-phase faults, adopted for this study, is as follows:

- 1st stage: 120 ms (instantaneous + 120 ms, the response time of the equipment for opening)
- 2nd stage: 520 ms (400 ms + 120 ms, the response time of the equipment for opening).

These times for eliminating three-phase faults are considered the baseline hypothesis of this study. The network parameters, namely the characteristics of the lines and transformers, made it possible to model and configure the elements in the Powerfactory simulation software.

B. Model Validation

The validation of the complete model relies on two complementary approaches. On the one hand, the individual components (PV, batteries, converters) were validated by comparison with the manufacturer's data. On the other hand, the overall behavior of the system was verified through compliance tests with IEC standards, particularly the IEC 60909 standard for short-circuit currents.

C. Optimization of Sizing

The optimization of sizing aims to determine the ideal configuration of the hybrid storage system (lithium-ion batteries + supercapacitors) for a 25 MWc grid-connected PV system. This optimization must reconcile two main objectives: minimizing the total system costs and reducing the energy imported from the grid. The challenge is to find the best compromise between these two often contradictory criteria, while respecting the technical and operational constraints of the system.

a. Problem Formulation

The optimization problem is formulated as a multi-objective one, defined by the following functions (11) and (12) and (13):

$$f_1(X_1, X_2) = c_{bat}x_1 + c_{sc}x_2 + c_{imp}P_{imp} \quad (11)$$

$$f_2(X_1, X_2) = P_{imp} \quad (12)$$

With:

· c_{bat} : unit cost per MWh for the battery.

· c_{sc} : unit cost per MWh for supercapacitors.

· c_{imp} : unit cost per imported MWh.

· P_{imp} : total energy imported (in MWh).

- The total energy import:

$$f_1(X_1, X_2) = P_{imp} \quad (13)$$

We need to minimize the total cost f_1 and imported energy f_2.

b. Technical Constraints

The problem is subject to several essential constraints to ensure technical feasibility.

- Constraints on the decision variable limits are defined in equations (14) and (15):

$$10 \le x_1 \le 16 \quad (14)$$

$$1 \le x_2 \le 4 \quad (15)$$

These limits ensure that the solutions remain within technologically feasible ranges. The proportion of supercapacitors compared to the total capacity is expressed in equation (16), using ($x_1 + x_2$).

$$0,05 \le \frac{x_2}{x_1 + x_2} \le 0,2 \quad (16)$$

This constraint ensures a balance between the two storage technologies.

- The minimum storage levels of batteries and supercapacitors, required for SoC management, are specified in equations (17) and (18):

$$SOC_{bat} > 0.3x_1 \quad (17)$$

$$SOC_{sc} \ge 0.1x_2 \quad (18)$$

- Equations (19) and (20) define the limits on the charging and discharging rates of the storage components:

Battery: $|P_{bat}| \le 20MW$ (19)

Supercapacitors: (20)

- Energy import limit:

©2006-2026 Asian Research Publishing Network (ARPN). All rights reserved.

At each time step, the following condition must be satisfied (21):

$$P_{imp} \leq 100MW \quad (21)$$

c. Methodology NSGA II

The choice of the NSGA-II algorithm is based on previous experiments, where it was successfully applied to the optimization of a diesel-storage hybrid production system for powering an isolated BTS station [16]. Its effectiveness in solving multi-objective problems with technical constraints motivated its use here.

The NSGA-II genetic algorithm is applied with the parameters:

- Population: 300 individuals
- Generations: 50 iterations
- Crossing: 80% probability
- Mutation: 5% probability
- Fitness: Calculated via MATLAB

Key process

- Initial random generation within the bounds
- Evaluation of objectives through numerical simulation
- Pareto front ranking

d. Optimization Results

The NSGA-II algorithm (Non-dominated Sorting Genetic Algorithm II) was chosen for its ability to effectively handle multi-objective problems. Its operation is based on:

Initial population: Random generation of 300 candidate solutions.

Evaluation: Each solution is tested through MATLAB/Power Factory coupled simulations.

Ranking: The solutions are sorted according to their Pareto dominance.

Selection: The best solutions are chosen based on their crowding distance, promoting diversity.

The algorithm iterates over 50 generations to converge towards an optimal Pareto front, offering a set of solutions balanced between cost and performance.

Figure-13 illustrates the optimal pareto front obtained from the optimization process.

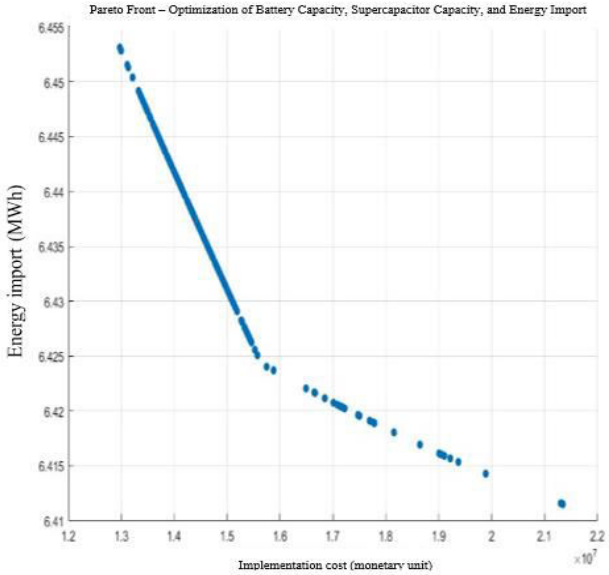


Figure-13. Optimal Pareto.

The chosen optimal solution is presented in Table-2 below:

Table-2. Optimization results.

Parameter	Value
Battery Capacity	13.50 MWh
SC Capacity	1 MWh
Total Cost	14.1 million XOF
Imported Energy	64.4 GWh

3. RESULTS AND CONVERSATIONS

A. Energy Management

The approach adopted for the management of the hybrid energy storage system (HESS) relies on leveraging the complementary characteristics of the two technologies used, namely a lithium-ion battery and a supercapacitor.

This complementarity allows for the optimization of the management of stored power and energy, taking into accounts the specific capacities and limitations of each technology.

The storage strategy primarily aims to meet the load demand by utilizing renewable energy sources and imports.

In our study, the power balance, denoted as, is defined as the difference between the power provided by the photovoltaic source (PV) and importation, on the one hand, and the power demanded by the load, on the other hand. A positive power balance indicates an energy surplus from the PV system and imports, while a negative balance indicates a power deficit, corresponding to a demand not covered by these two sources.

The algorithm governing the storage strategy is presented in Figure-14. Its operating principle is as

©2006-2026 Asian Research Publishing Network (ARPN). All rights reserved.

follows: when the energy sources do not fully meet the load demand, the missing energy is first supplied by the battery. If the latter is not sufficient in case of a demand peak, the supercapacitor takes over to cover the remaining deficit. Moreover, in the event of a surplus in photovoltaic production, the excess is primarily stored in the battery, and then in the supercapacitor if the battery reaches its limits. However, if neither of the two storage units can absorb the entire surplus, the difference is injected into the grid.

Thus, although the two SSEH adopt a common management strategy, their respective constraints in terms of SOC and maximum power impose distinct operating conditions.

In this study, the management strategy is evaluated through a simulation applied to the interconnected network of Benin, but on a smaller scale. The analysis area is limited to the 161 kV substation in Onigbolo, as well as the surrounding substations of the same voltage level. This approach allows for observing the system's behavior in a realistic context while managing the complexity of modeling.

The algorithm detailed in Figure-14 relies on several equations modeling the performance and limitations of the storage system. The efficiency of the battery cycle and that of the AC/DC power converter allow for estimating the actual exchanged power, regardless of the dynamic constraints of SOC and power.

The maximum charging and discharging powers are determined based on the maximum C-rate during charging and discharging, as well as the nominal capacity of the storage (expressed in Ah) and its voltage, assumed to be almost constant over a one-minute time step due to the system's large capacity. On the other hand, no power limitation has been imposed on the supercapacitor. Finally, the unmet power is evaluated based on the remaining power $P_{restant}(t)$, calculated taking into account efficiency losses and the total exchanged power $P_{exch}(t)$.

This SSEH management algorithm, as presented, is designed to run in a loop as long as the system is active. The charging and discharging of the components are adjusted based on several predefined parameters. After separately analyzing the operation during charging and discharging of the two storage systems as well as the energy management within the system, highlighting the storage performance and its impact on the optimization of energy flows, it is prudent to simulate the entire system over a given period through a quasi-dynamic charge flow in order to analyze the complementarity of the different components, namely: photovoltaic power plant, interconnected grid, battery, and supercapacitor. It is also crucial to evaluate the dynamic stability of the network. Indeed, the integration of batteries and supercapacitors, although effective for energy regulation, can also introduce complex dynamics that influence the overall behavior of the system. The following section therefore focuses on the study of these different aspects.

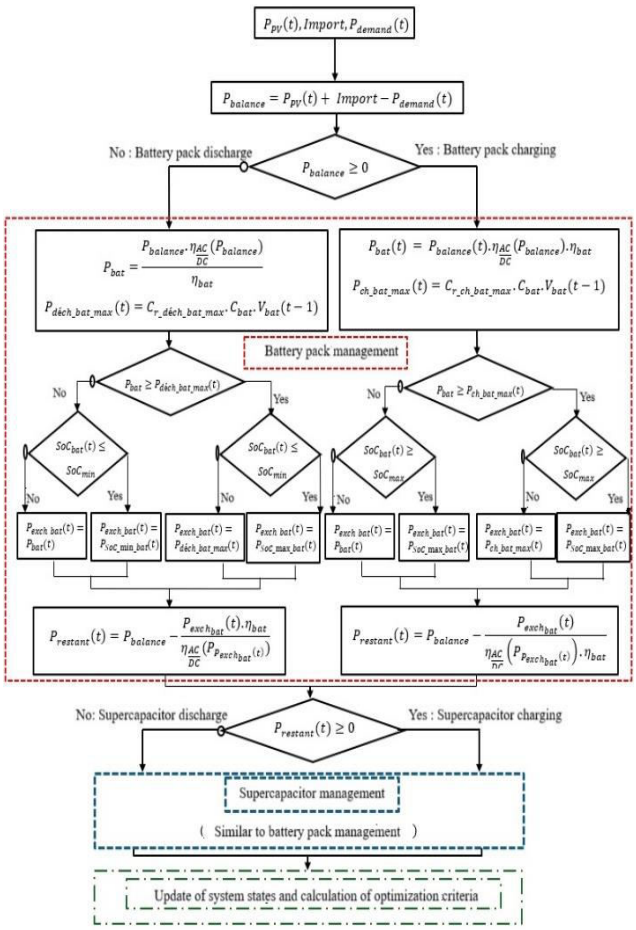


Figure-14. Management Algorithm.

B. RESULTS AND DISCUSSIONS

a) Analyse Battery Charge

The simulations in this section aim to demonstrate the charging and discharging operation of the storage devices. These are charged during the day during the production period, and discharge is only observed at the night time peak of the study area. The simulations for the battery were conducted according to the predefined conditions below (22):

- Load conditions

$$\begin{cases} Discharge = 0 \\ SOC < 100 \\ Irradiation_G > 300W/m^2 \end{cases} \Rightarrow Load = 1 \quad (22)$$

©2006-2026 Asian Research Publishing Network (ARPN). All rights reserved.

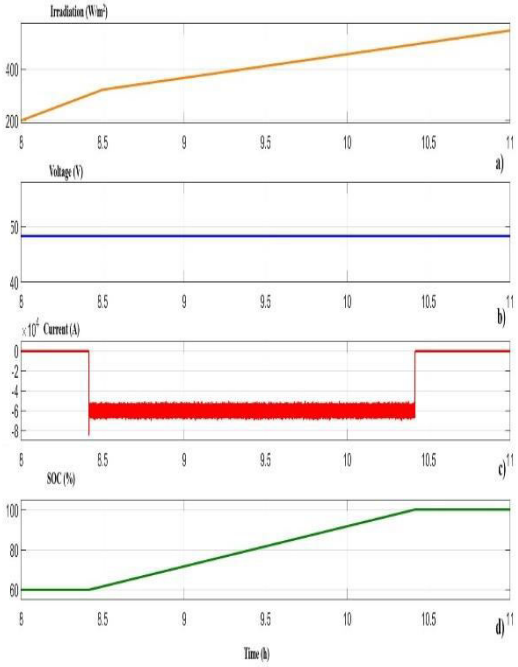


Figure-15. Battery charge curves a) Irradiation, b) Voltage, c) Current, d) SOC.

The observation of the charging cycles reveals a direct correlation between solar irradiation and energy accumulation in the battery (Figure-15). At 8 AM, although the battery has an initial state of charge of 60% (approximately 8.1 MWh available out of 13.5 MWh), the low irradiation (200 W/m²) does not allow the charging to start. This behavior reflects an intelligent trigger threshold that avoids drawing on storage as long as the photovoltaic production remains insufficient to ensure an effective charge. A little before 8:30, with irradiation exceeding 300 W/m², the battery begins to charge at a current reaching 60 kA. The rapid charging allows for the efficient use of available solar energy, thus avoiding losses of unstored energy.

The charging duration extends over 2 hours and 5 minutes (from 8:20 AM to 10:25 AM), thus reaching the full capacity of 13.5 MWh. As soon as the maximum charge level is reached, the charging current becomes zero. Throughout this process, the voltage across the storage terminals remains stable at 48.3V, which confirms effective management of load variations.

b) Battery Discharge Analysis

Figure-16 below shows the different curves obtained during the partial discharge test of the battery (Voltage, Current, and SOC) (23).

- Discharge conditions

$$\begin{cases} 18h < t < 22h \\ SOC > 70 \end{cases} \Rightarrow Discharge = 1 \quad (23)$$

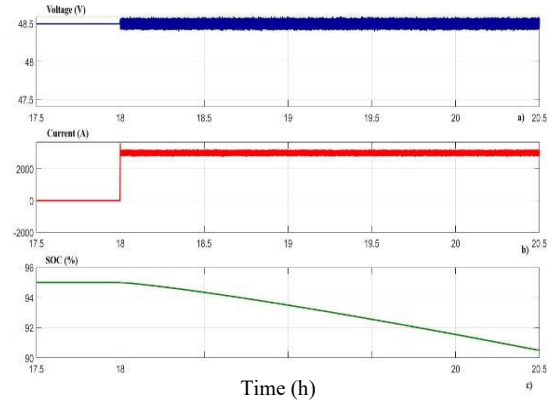


Figure-16. Battery discharge curves a) Voltage, b) Current, c) SOC.

Figure-17 shows the three-phase voltages of the inverter, and Figure-18 provides a zoom of these same three-phase voltages.

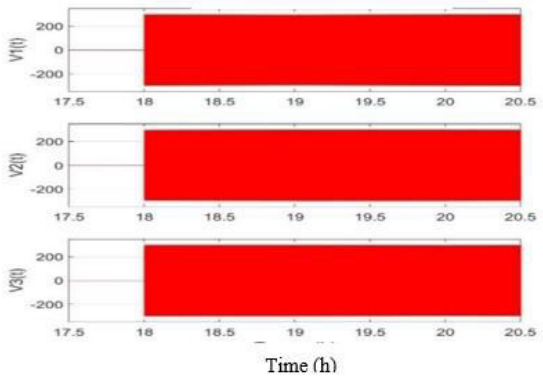


Figure-17. Inverter voltage.

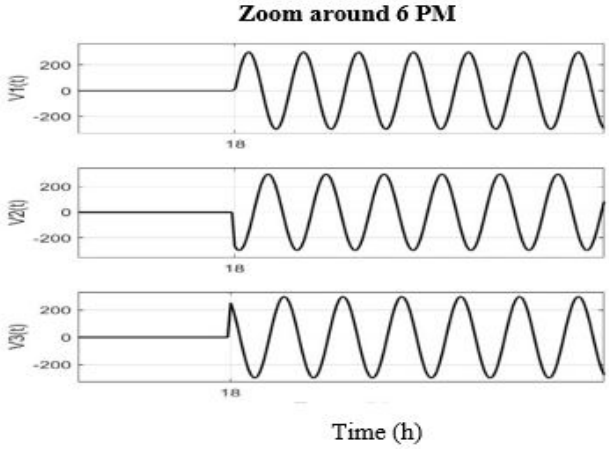


Figure-l8. Focus on the inverter voltage.

©2006-2026 Asian Research Publishing Network (ARPN). All rights reserved.

The role of the battery is not limited to storage alone, but extends to a significant reduction in dependence on the external power grid. At 5:30 PM, although the battery shows a state of charge of 95% (approximately 12.8 MWh stored), no discharge is initiated immediately. This suggests a time optimization strategy where the battery is only mobilized during peak periods when demand is high starting at 6 PM, the battery begins to discharge with a current of 2.8 kA, powering an average load of 11 MW.

The associated inverter (Figure-17) converts the energy into a three-phase voltage, ensuring a stable power supply to the connected equipment. Between 6 PM and 8:30 PM, the battery delivers approximately 4% of its total capacity, or 0.54 MWh, which helps to lighten the load on the grid and delay the import of electricity.

The battery thus plays a role as an energy buffer, providing a significant amount of energy that helps reduce the reliance on imports from the grid. At full charge (13.5 MWh), it could theoretically supply the average load of 11 MW for more than an hour, which provides a valuable window to adjust production and minimize electricity supply costs.

c) Supercapacitor Results

The analysis of the behavior of the supercapacitor, with a capacity of 1 MWh, highlights its essential role in managing power peaks and optimizing the system's energy consumption by ensuring a rapid response to load variations.

The simulations for the supercapacitor were conducted according to the predefined conditions below (24) and (25):

- Load condition

$$\begin{cases} Discharge = 0 \\ SOC < 100 \\ P < 12,5MW \end{cases} \Rightarrow Load = 1 \quad (24)$$

- Discharge condition

$$\begin{cases} P > 12,5MW \\ SOC > 70 \end{cases} \Rightarrow Discharge = 1 \quad (25)$$

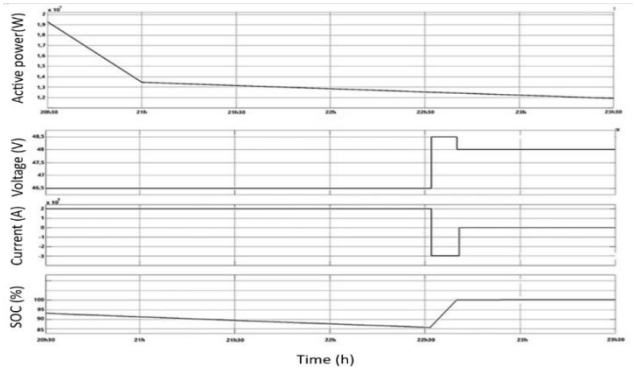


Figure-19. Operation of the supercapacitor a) Active Charge, b) Voltage, c) Current, d) SOC.

a. Analysis of the Supercapacitor Discharge Process

The activation of the supercapacitor is directly conditioned by the active power of the grid. At 8:30 PM, when the load exceeds a certain limit (above the critical threshold of 12.5 MW), the supercapacitor is mobilized to compensate for the peak demand and thus reduce the need to import surplus energy from the external grid.

This buffer role is crucial to ensure a stable supply without immediately tapping into other energy sources.

During this discharge phase, which extends from 8:30 PM to 10:35 PM, the state of charge (SOC) of the supercapacitor decreases from 93% to 86%, corresponding to a discharge of 7% of its total capacity, or approximately 70 kWh.

This amount of injected energy significantly helps to alleviate the network overload, avoiding an increase in import costs and delaying the activation of more expensive sources.

The associated inverter ensures an efficient conversion of the stored energy, delivering a simple effective three-phase voltage of 230V. The analysis of the waveforms at the inverter output shows voltage stability and a discharge current of 2 kA, confirming the proper functioning of the system. The voltage of the supercapacitor evolves to 46.5V during discharge, slightly lower than its nominal voltage of 48V, which remains in line with the operating characteristics of supercapacitors.

b. Analysis of the Supercapacitor Charging Process

In order to better manage the data in Simulink and observe the operation of the supercapacitor, we have combined its discharge followed by its charge as shown in figure 19. As soon as the active power drops below the threshold of 12.5 MW at 10:35 PM, the supercapacitor charging begins. The objective is to replenish its energy stock so that it can respond effectively to the next load fluctuations. This recharging cycle is particularly fast, lasting only 5 minutes (from 10:35 PM to 10:40 PM), which demonstrates the supercapacitor's ability to recharge much more quickly than a conventional battery. The charging current reaches approximately 3 kA, accompanied by a voltage that rises to 48.5V, which is a

©2006-2026 Asian Research Publishing Network (ARPN). All rights reserved.

slight overvoltage at the time of charging. Once the SOC returns to 100%, the charging current becomes zero, and the voltage stabilizes at 48V, its nominal voltage. The supercapacitor is then ready to be used again during the next peak in consumption.

C. Power Flow

The purpose of this study is to analyze the quasi-dynamic operation of the electrical system, taking into account the Onigbolo photovoltaic power plant, battery storage systems, and supercapacitor systems.

The simplified model of the network around the Onigbolo node, showing the main import source, solar production, the various incoming and outgoing lines, storage devices, and the load, is illustrated in Figure-20 below.

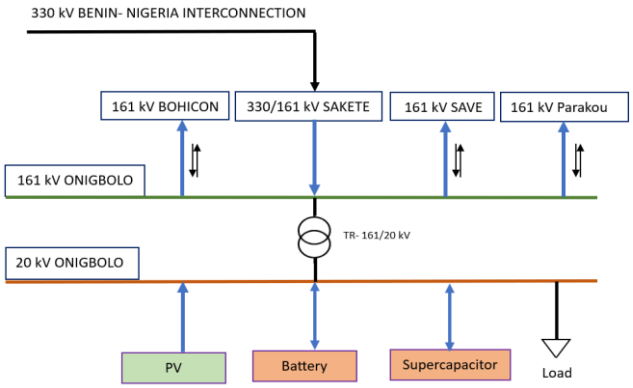


Figure-20. Simplified diagram.

a. Results of Charge Flow in Quasi-Dynamic Operating Regime (QDSL)

The quasi-dynamic load flow (QDSL) allows for the analysis of the evolution of power flows in the network on an intermediate time scale between the static regime and the complete dynamic regime. Here, photovoltaic solar production and storage solutions are integrated into the network to analyze their contributions during periods of demand fluctuations according to various scenarios. The balance at the 20kV busbar, the connection point of the power plant and storage devices, will be the main node to observe.

- Initial situation without storage systems

This involves analyzing the power flow of the network in its initial state without the contribution of storage. A simulation over a period of one day is therefore carried out.

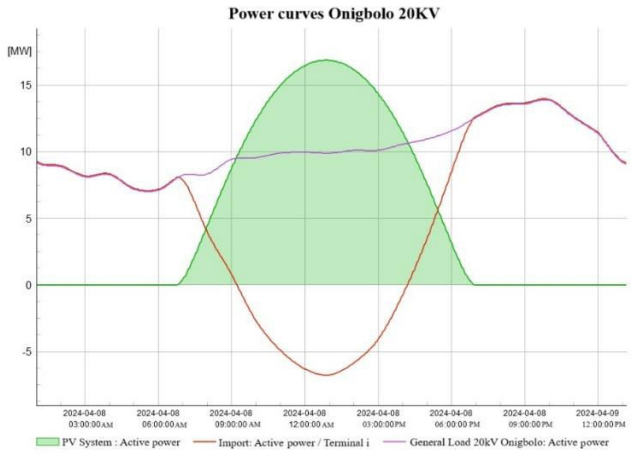


Figure-21. Power curves Onigbolo 20kV (without storage).

Figure-21 above respectively illustrates the curves of photovoltaic solar production (green) which follows a classic daily cycle with a peak of about 16.8 MW; the grid load (purple) relatively stable between 7 and 13.45 MW, and the import (red) which represents the consumption profile on the 20kV busbar.

The analysis of the curves reveals that power importation (red curve) varies in opposition (gradually decreases) with solar production (green curve) when the latter increases during the day.

Conversely, in the absence of solar production (night and early morning), import remains the main source that supplies the station's loads, which reflects the normal situation of the network. It should be noted that the import at this node is strongly compensated by solar production during the day, but the dependence on the grid remains significant outside of production hours.

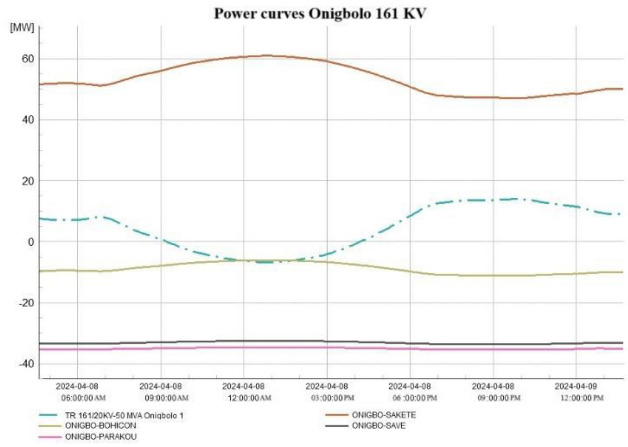


Figure-22. Power curves Onigbolo 161kV (without storage).

The 161 kV network ensures system stability by compensating for production and consumption fluctuations at the 20 kV node in the absence of energy availability limitations. As illustrated in Figure-22 above, the

©2006-2026 Asian Research Publishing Network (ARPN). All rights reserved.

integration of solar power reduces the load on the transformers and decreases the power demand on the 161kV network, although inter-substation exchanges remain generally stable. The power transit curves on the Onigbolo-Parakou, Onigbolo-Sakété, and Onigbolo-Savè lines indicate power exchanges between Onigbolo and other network substations. These flows are relatively stable, showing the impact of PV production on the 161 kV network.

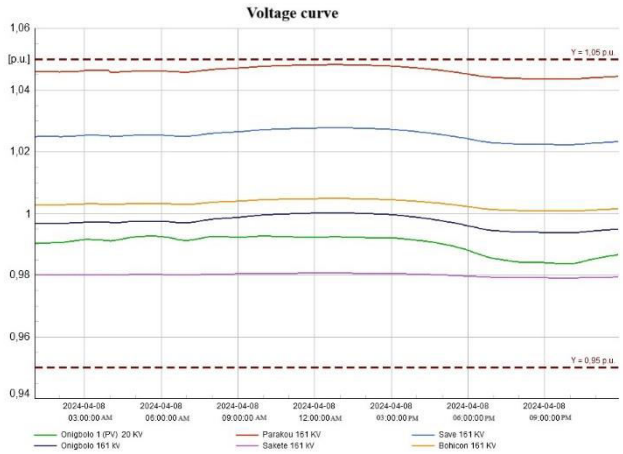


Figure-23. Voltage profile (without storage).

The graph in Figure-23 above shows the voltages at the nodes of the different substations following the load flow performed on the network in its initial state.

These are the substations Onigbolo, Parakou, Sakété, Bohicon, and Savè present in the study area.

The analysis of these voltage curves highlights, as summarized in Table-3 below, the stability of the network within the admissible operating range (0.95 to 1.05 p.u.).

Table-3. Range of tensions observed.

Nodes	Observed voltage range (p.u.)	Recommended range (0.95 - 1.05 p.u.)
Onigbolo 1 (PV) 20 kV (Green)	0,98 - 1	✓ Good (on the beach)
Onigbolo 161 kV (Blue)	0,99 - 1,01	✓ Good (on the beach)
Parakou 161 kV (Red)	1,04 - 1,05	✓ Good (upper limit)
Sakété 161 kV (Violet)	0,97 - 0,98	✓ Good (on the beach)
Save 161 kV (Light blue)	1,02 - 1,03	✓ Good (on the beach)
Bohicon 161 kV (Orange)	1 - 1,01	✓ Good (on the beach)

- Situation with battery storage

Figure-24 below presents the power flow study conducted over 24 hours in the presence of the battery, import, and photovoltaic power plant.

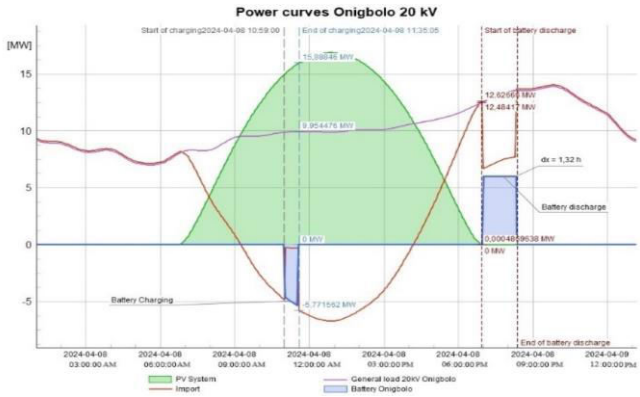


Figure-24. Power curves Onigbolo 20kV (With battery).

©2006-2026 Asian Research Publishing Network (ARPN). All rights reserved.

As previously illustrated and as shown in the graph in Figure-24 above, power importation (red curve) varies oppositely (gradually decreases) with solar production (green curve) when the latter increases during the day. During this production period, which covers the demand at this node, the battery charges as shown in the figure.

At the peak of consumption on the node, the battery begins its discharge at 7 PM for a duration of one hour and thirty-two minutes, thereby helping to reduce energy imports.

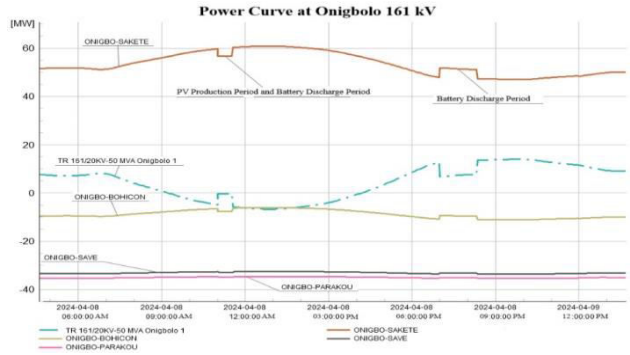


Figure-25. Power curves Onigbolo 161kV (With battery).

The blue curve (TR 161/20 kV-50 MVA Onigbolo 1) in Figure-25 above indicates how the active power of import is influenced by solar production. The decrease in power in the middle of the day corresponds to a period of solar production, thereby reducing the demand on the transformer. The dips observed on certain curves therefore indicate the periods when we have contributions from the batteries in charging and discharging.

Figure-25 below shows the evolution of the voltage at the different nodes for this simulation case.

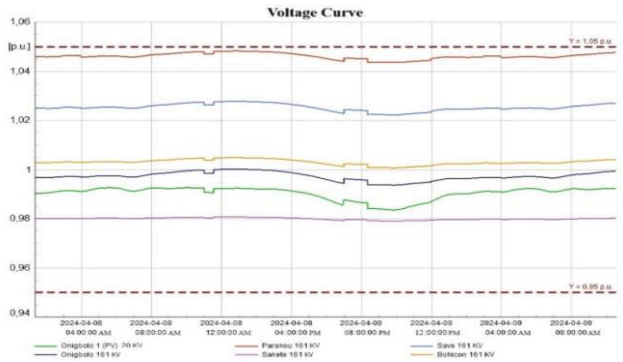


Figure-26. Voltage profile.

It is easy to observe from the curves in Figure-26 above, whose data is summarized in Table-4 below, that the voltages of the different nodes in the network comply with the announced planning limits.

Table-4. Range of tensions observed.

Nodes	Observed voltage range (p.u.)	Recommended range (0.95 - 1.05 p.u.)
Onigbolo (PV) 20 kV	0,98 - 1	✅ Good (on the beach)
Onigbolo 161 kV	0,99 - 1,01	✅ Good (on the beach)
Parakou 161 kV	1,04 - 1,05	✅ Good (on the beach)
Sakété 161 kV	0,97 - 0,98	✅ Good (on the beach)
Save 161 kV	1,02- 1,03	✅ Good (on the beach)
Bohicon 161 kV	1 - 1,01	✅ Good (upper limit)

- SITUATION WITH THE BATTERY AND THE SUPERCAPACITOR

- Power flow

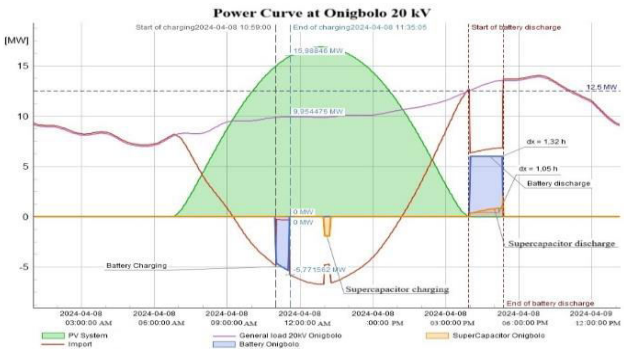


Figure-27. Power curve at Onigbolo 20kV (With battery and supercapacitor).

©2006-2026 Asian Research Publishing Network (ARPN). All rights reserved.

As previously observed and explained for the production and charging of the battery, we can see from the graph in Figure-27 above that the supercapacitor also charges during the day in periods of solar production and begins its discharge in this case from the peak exceeding 12.5MW, accompanying the battery to compensate for imports.

The graph thus shows how solar production, the battery, and the supercapacitor interact to balance the supply and demand of energy in Onigbolo, thereby reducing the need to import a large amount of energy.

The curves in Figures 28 and 29 below respectively show the state of charge of the two storage devices and their stored energy flows.

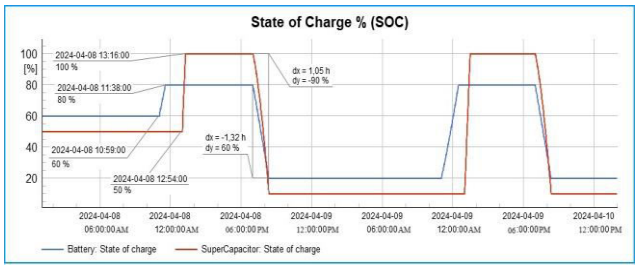


Figure-28. State of Charge.

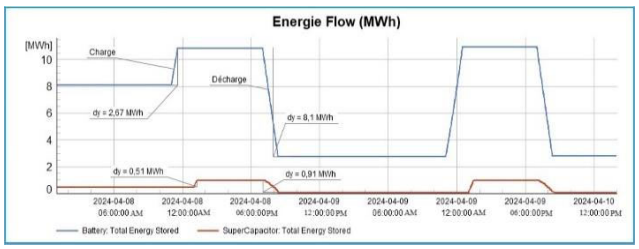


Figure-29. Energy Flow of Storage Systems.

The graph in Figure-28 highlights the charging and discharging cycles of the battery (state of charge), thus showing the charging and discharging rates of the two storage systems, namely the battery (blue curve) and the supercapacitor (red curve). This reflects the principle of energy accumulation during the PV production period and energy restitution during the peak period. As for the graph in Figure-29, it highlights the flows of stored and released energy during the charging and discharging phases, respectively.

The blue curve in Figure-28, that of the battery, shows that the state of charge goes from an initial rate of 60% to 80% for a stored energy of approximately 2.67 MWh as illustrated in the curve of Figure-29 during the charging period on the first day. At the same time, the supercapacitor goes from a charge rate of 50% to 100% (Figure-28, red curve) for a stored energy of 0.51 MWh (Figure-29, red curve) during the charging period. Furthermore, for the discharge during the nighttime peak period, the battery supplied 60% of its energy (Figure-28) to the grid, which corresponds to 8.1 MWh (Figure-29) of energy returned during the peak period.

It should be noted that the battery's dynamics are part of a medium- and long-term storage strategy, essential for smoothing supply variations and optimizing system use. The supercapacitor, for its part, delivered 90% of its energy, which corresponds to 0.51 MWh, in support of the battery system to handle the peak demand. Its role is primarily to provide compensation by managing power peaks and attenuating rapid network variations, which also contributes to the overall stability of the system.

The power curves at the 161 kV network level are illustrated in Figure-30 below.

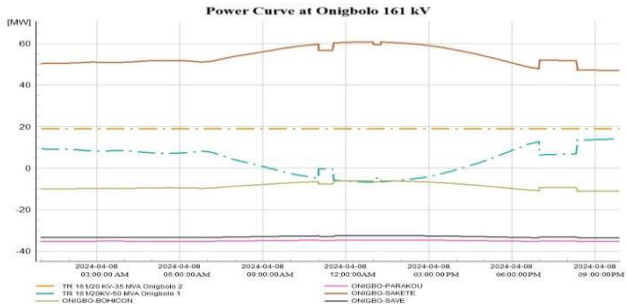


Figure-30. Power curves for Onigbolo 161kV.

These curves illustrate the dynamics of the network based on the power flow, highlighting the contribution of photovoltaic production as well as the charge and discharge cycles of storage devices. Moreover, the evolution curves of the tensions at the different nodes, as shown in Figure-31 below, also reflect the behaviors observed and discussed previously.

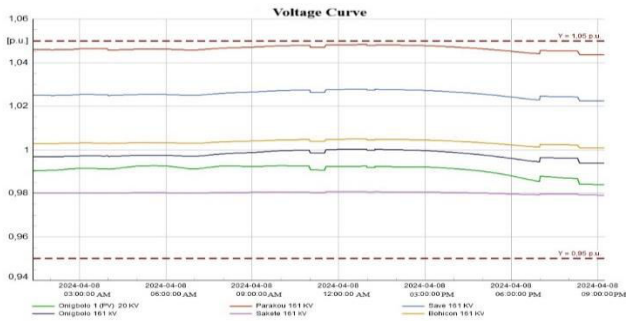


Figure-31. Voltage profile (With battery and supercapacitor).

These curves show that the normal voltage limit ranges are respected at all nodes of the network in the study area.

Following the various analyses conducted on the network's behavior in terms of power flow and available energy management, it is essential to deepen the study through a dynamic analysis, incorporating disruptive events such as short circuits, to assess the impact of the photovoltaic power plant and storage devices on the stability and resilience of the electrical grid.

Tables 5 and 6 below respectively show the power contributions of the hybrid battery plus

©2006-2026 Asian Research Publishing Network (ARPN). All rights reserved.

supercapacitor system as well as the voltages at the different nodes with and without said system.

The different values are taken at specific hours belonging to the nighttime peak of the network with a spacing of 30 minutes.

Table-5 perfectly shows the contribution of storage through the reduction of imports when the hybrid system operates. At the same time, Table-6 shows the low impact of storage on voltage variation. The latter remains very low or almost zero at certain nodes during the operation of the hybrid storage system compared to the initial situation of the network without storage.

Table-5. Summary of power contribution.

Without battery & without supercapacitor					
Quasi-dynamic AC simulation	**PV System (MW)**	**Importation (MW)**	**General load 20kV Onigbolo (MW)**	**Onigbolo Battery (MW)**	**Super Condo Onigbolo (MW)**
2024.04.08 06.00.00 PM	3,1	8,5	11,6	0	0
2024.04.08 06.30.00 PM	1,1	11,0	12,0	0	0
2024.04.08 07.00.00 PM	0	12,6	12,6	0	0
2024.04.08 07.30.00 PM	0	13,1	13,1	0	0
2024.04.08 08.00.00 PM	0	13,5	13,5	0	0
2024.04.08 08.30.00 PM	0	13,6	13,6	0	0
With battery & supercapacitor					
2024.04.08 06.00.00 PM	3,1	8,6	11,6	0	0
2024.04.08 06.30.00 PM	1,0	11,0	12,0	0	0
2024.04.08 07.00.00 PM	0	6,2	12,6	6,00	0,4
2024.04.08 07.30.00 PM	0	6,5	13,1	6,00	0,6
2024.04.08 08.00.00 PM	0	6,7	13,5	6,00	0,8
2024.04.08 08.30.00 PM	0	13,6	13,6	0	0

©2006-2026 Asian Research Publishing Network (ARPN). All rights reserved.

Table-6. Summary of tensions at the nodes.

Without battery and without supercapacitor						
Quasi-dyna Mic AC simulation	**Onigbolo 1 (PV) 20 kV p.u.**	**Onigbolo 161 kV p.u.**	**Parakou 161 kV p.u.**	**Sakete 161 kV p.u.**	**Savè 161 kV p.u.**	**Bohicon 161 kV p.u.**
2024.04.08 06.00.00 PM	0,988	0,996	1,045	0,980	1,024	1,002
2024.04.08 06.30.00 PM	0,987	0,995	1,045	0,980	1,023	1,002
2024.04.08 07.00.00 PM	0,985	0,994	1,044	0,979	1,023	1,001
2024.04.08 07.30.00 PM	0,985	0,994	1,044	0,979	1,023	1,001
2024.04.08 08.00.00 PM	0,984	0,994	1,044	0,979	1,023	1,001
2024.04.08 08.30.00 PM	0,984	0,994	1,044	0,979	1,022	1,001
With battery and supercapacitor						
Quasi-dynamic AC simulation	Onigbolo 1 (PV) 20 kV p.u.	Onigbolo 161 kV p.u.	Parakou 161 kV p.u.	Sakete 161 kV p.u.	Save 161 kV p.u.	Bohicon 161 kV p.u.
2024.04.08 06.00.00 PM	0,988	0,996	1,045	0,980	1,024	1,002
2024.04.08 06.30.00 PM	0,987	0,995	1,045	0,980	1,023	1,002
2024.04.08 07.00.00 PM	0,988	0,996	1,046	0,980	1,025	1,002
2024.04.08 07.30.00 PM	0,987	0,996	1,045	0,980	1,024	1,002
2024.04.08 08.00.00 PM	0,987	0,996	1,045	0,980	1,024	1,002
2024.04.08 08.30.00 PM	0,984	0,994	1,044	0,979	1,022	1,001

D. Short-Circuit Results

This section aims to verify the impact of maximum short-circuit currents from the solar park and storage systems on the upstream network.

The different simulated events and the illustration of the principle are presented respectively in Figure-32 and Figure-33 as follows:

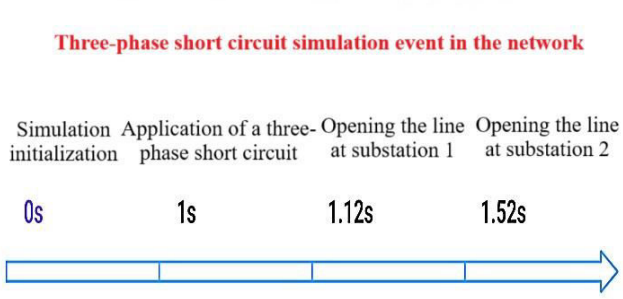


Figure-32. Events of three-phase short-circuit simulation in the network.

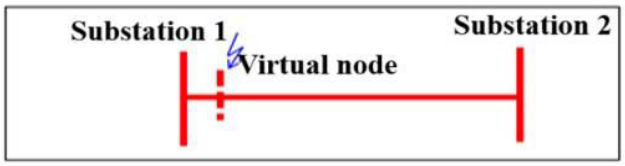


Figure-33. Illustration of the principle.

0s → 1s: Initialization

The simulation starts at the 0 second mark.

During the first second, the system is initialized. This means that the initial conditions of the network are defined (voltages, currents, etc.).

1s: Application of a Three-Phase Short Circuit at the Dummy Node At 1 second, a three-phase short circuit is applied to a fictitious node.

1s → 1.12: Simulation Between 1 second and 1.12 seconds, the simulation is executed with the short circuit applied. During this period, the effects of the short circuit on the network are simulated.

1.12s: Opening of the Line on the Post 1 Side

©2006-2026 Asian Research Publishing Network (ARPN). All rights reserved.

At 1.12 seconds, the power line is open on the side of station 1.

The opening of the line is probably a protective action to isolate the defect.

1.12s → 1.52s: Simulation Between 1.12 seconds and 1.52 seconds, the simulation continues with the line open. During this period, the network behavior after the line opening is simulated.

1.52s: Opening of the Line on the Post Office Side 2.

At exactly 1.52 seconds, the power line is also open on the side of station 2. This completely isolates the section of the line where the defect was simulated.

The simulated cases are listed as follows:

- Loss of the Onigbolo-Bohicon line (fault on the Onigbolo side, 8:30 PM)
- Loss of the Onigbolo-Bohicon line (fault on the Bohicon side, 8:30 PM)
- Loss of the Onigbolo-Bohicon line (fault on the Onigbolo side, 2:30 PM)
- Loss of the Onigbolo-Bohicon line (fault on the Bohicon side, 2:30 PM)

These different cases are simulated in an initial situation (without the solar power plant and without the storages) and in a second situation (with the solar power plant and the storages). However, we will only present the results of the fault on the Onigbolo side, the station benefiting from the new solutions.

a. Initial Situation without the Solar Power Plant and Without Storage

- Loss of the Onigbolo-Bohicon line (fault at 1s on the Onigbolo side, 8:30 PM)
- Contribution of the power plants

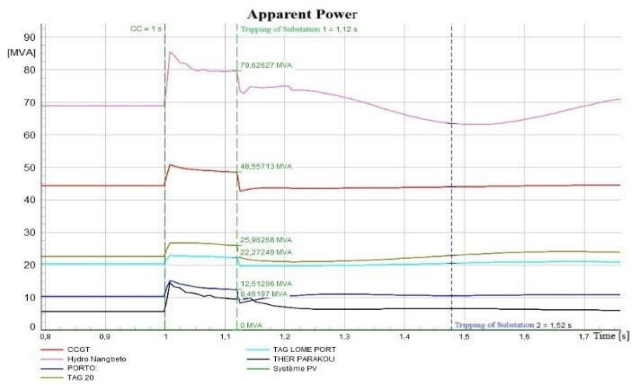


Figure-34. Apparent power.

The graph in Figure-34 above illustrates the dynamic response of the grid following the loss of the Onigbolo-Bohicon line in the absence of the solar power plant and storage devices. A sharp increase in the apparent power supplied by the existing plants is observed immediately after the fault (t = 1s), reflecting their response to compensate for the line loss. The contributions of the different plants vary depending on their capacity and location in the network, with plants like CCGT and Hydro Nangbéto recording the highest power peaks. The triggering of the stations at 1.12s and 1.52s marks the steps of network protection, aiming to isolate the disturbance. This analysis highlights the system's sensitivity to the type of fault simulated in the absence of storage and PV production means.

- Contribution of the 161 kV lines

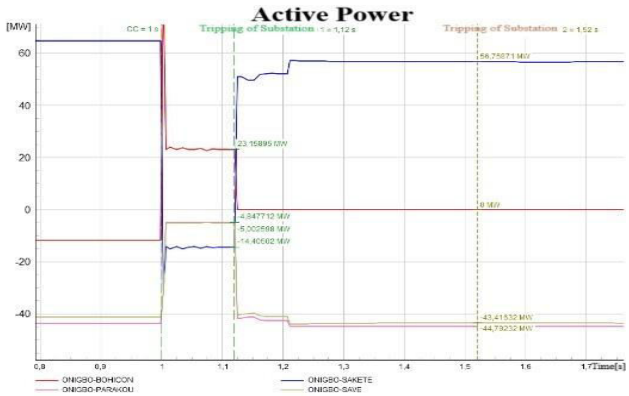


Figure-35. Active power of the lines.

The curves in Figure-35 represent the evolution of active power on the other 161 kV transmission lines during the loss of the Onigbolo-Bohicon line.

The impact of the fault at t = 1s (Onigbolo side) is marked by a strong variation in the power exchanged on the different lines, highlighting the effect of the disturbance on the network. After the activation of the first station at t = 1.12 s, a readjustment of the power flows is observed, notably with an increase in the power transmitted on certain lines and a decrease on others. The second trigger at t = 1.52 s partially stabilizes the flows as can be observed.

- Frequency of groups

©2006-2026 Asian Research Publishing Network (ARPN). All rights reserved.

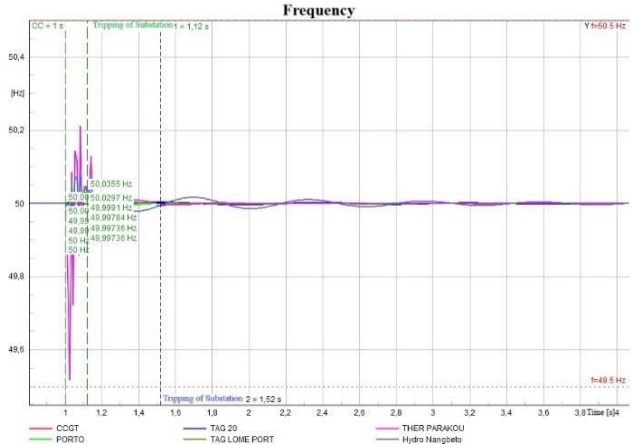


Figure-36. Frequency of groups.

Figure-36 above illustrates the evolution of the frequency of the generator groups during the loss of the Onigbolo-Bohicon line. The short circuit at t = 1 s (Bohicon side) induces a transient disturbance marked by frequency oscillations, reflecting the impact of the instantaneous imbalance between production and load. However, the peaks of these oscillations respect the permissible frequency limits as indicated on the graph.

After the activation of the first station at t = 1.12 s, the frequency begins to stabilize gradually, although residual variations remain.

The second trigger at t = 1.52 s contributes to a return to a quasi-nominal frequency around 50 Hz.
This analysis highlights the resilience of the network in the face of a line loss.

- Voltages at the bus stations

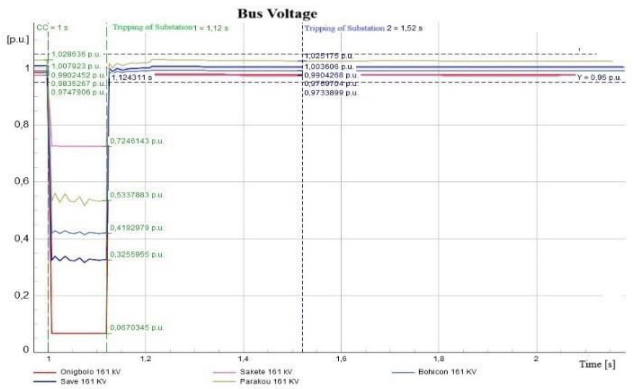


Figure-37. Evolution of tensions at the nodes.

This figure shows the evolution of voltages at the different buses of the network following the loss of the Onigbolo-Bohicon line.

The appearance of the short circuit at t = 1 s causes an instantaneous drop in voltages on certain buses, indicating a strong local disturbance. After the activation of the first station at t = 1.12 s, a beginning of voltage stabilization is observed, although some remain below the nominal value. The second trigger at t = 1.52 s allows for a gradual stabilization of the voltages, converging towards a range between 0.95 and 1.05 p.u. This situation reflects the normal behavior of a network of this size in the event of a fault.

- Loss of the Onigbolo-Bohicon line (fault at 1s on the Onigbolo side, 2:30 PM)

- Contribution of the power plants

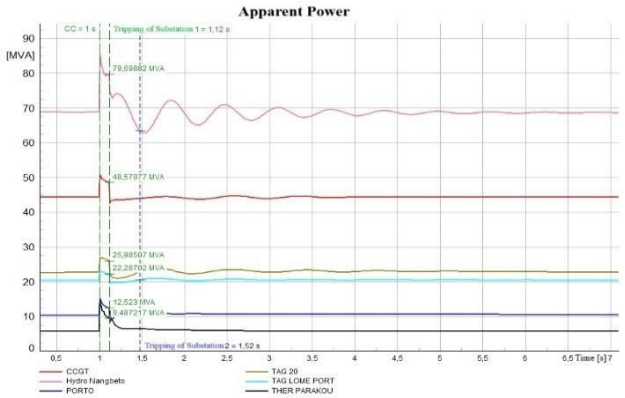


Figure-38. Apparent power.

Figure-38 illustrates the distribution of apparent power among the plants during the loss of the Onigbolo-Bohicon line, with a fault initiated at 2:30 PM (Onigbolo side). It is observed that at t = 1 s, the occurrence of the short circuit leads to an increase in the power supplied by certain production units, particularly the CCGT plant and the Nangbéto hydroelectric plant.

After the activation of the first station at t = 1.12 s, the powers begin to decrease, but with persistent oscillations until a gradual stabilization after t = 2 s. The second trigger at t = 1.52 s allows for a new equilibrium to be reached with more moderate power values.

- Contribution of the 161 kV lines

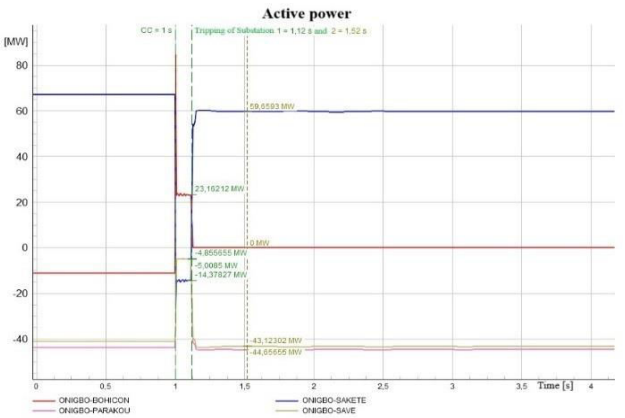


Figure-39. Active power of the lines.

©2006-2026 Asian Research Publishing Network (ARPN). All rights reserved.

This Figure-39 illustrates, as in the previous case, the dynamic response of the network in terms of active power following the simulated fault on the 161 kV lines, particularly regarding the contributions of the different lines connected to the Onigbolo substation. A significant variation in active power is observed immediately after the fault (t = 1s), as in the case simulated at 8:30 PM at the network peak, reflecting the network's response to compensate for the disturbance. The contributions of the different lines vary according to their capacity.

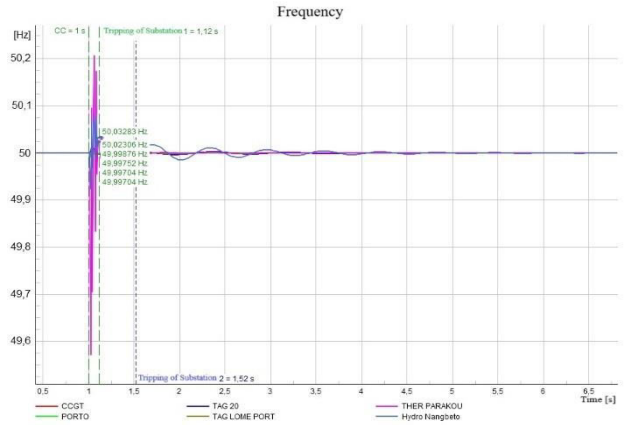


Figure-40. Frequency of groups.

The graph in Figuree-40 above illustrates the frequency response of the different power plants following the simulated fault on the grid, highlighting the fluctuations and stabilization of the electrical frequency after the event. A significant initial disturbance is observed at 1 second, where the frequency drops for all power plants. This drop is followed by a stabilization around 50 Hz after the triggering of the stations at 1.12 s and 1.52 s, as in the previous case.

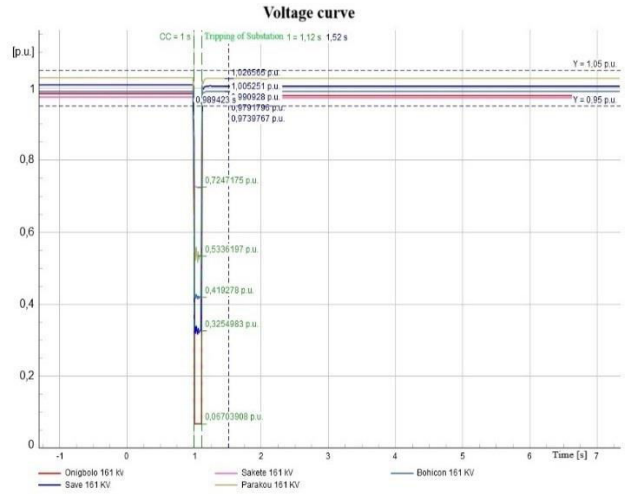


Figure-41. Evolution of tensions at the nodes.

The evolution of the voltage at the nodes of the different substations following the application of the short circuit in this scenario is illustrated in the graph of Figure-41 above.

The same stabilization behavior is observed after the triggers at 1.12 s and 1.52 s as in the previous case.

b. Situation with the Solar Power Plant and the Storage Facilities

- Loss of the Onigbolo-Bohicon line (fault at 1s on the Onigbolo side, 8:30 PM)
- Contribution of the power plants

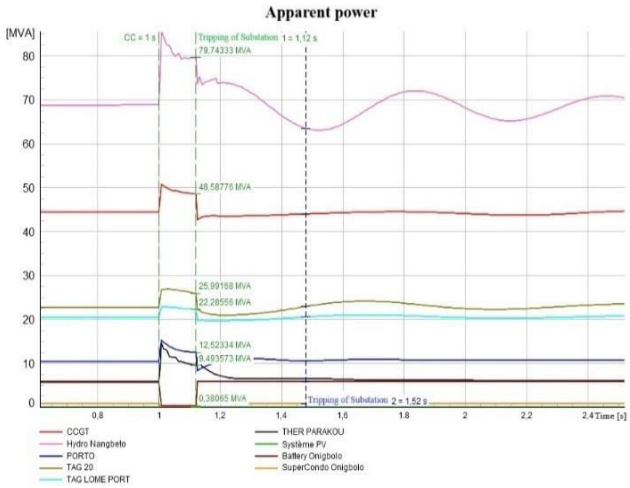


Figure-42. Apparent power.

The graph in Figure-42 above illustrates the dynamic response of the network following the simulated fault on the Onigbolo-Bohicon line at 8:30 PM, in the presence of the solar power plant (outside the production period) and the storage devices in discharge mode. A rapid reaction from the various plants is observed after the fault at 1 second, with an immediate increase in the apparent power supplied by the existing plants to compensate for the line loss and stabilize the grid.

The storage systems, such as batteries and supercapacitors, on the other hand, experienced an immediate drop in the power they were delivering at the moment of the short circuit and regained stability starting from 1.12 seconds.

Power fluctuations are better managed, and stabilization is just as quick as in the case simulated without storage devices. This shows that storage systems do not compromise network stability and contribute minimally to short circuits, thereby enhancing network efficiency.

- Contribution of the 161 kV lines

©2006-2026 Asian Research Publishing Network (ARPN). All rights reserved.

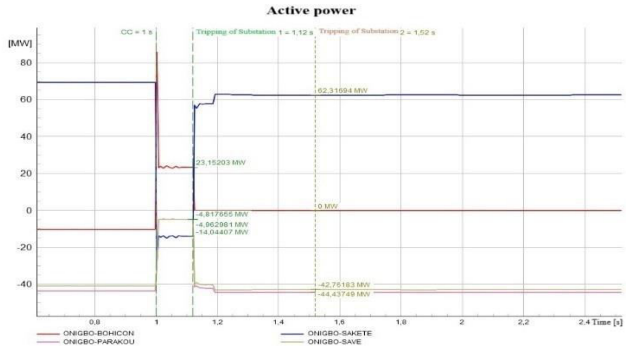


Figure-43. Active power of the lines.

The power curves at the line level, as illustrated in Figure-43 above, do not show significant divergence points compared to the fault case studied without energy storage at the same peak hour.

- Frequency of groups

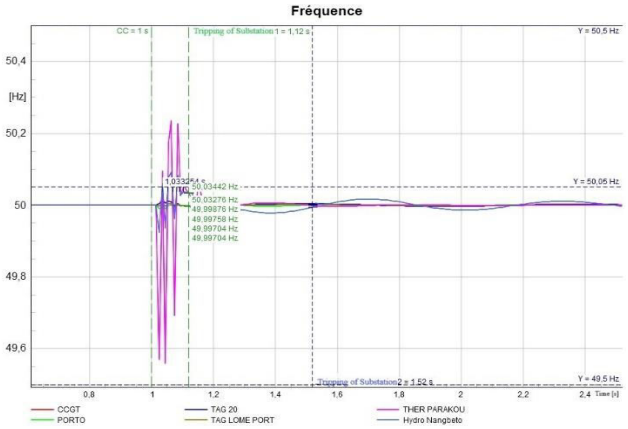


Figure-44. Frequency of groups.

We observe in the curves of Figure-44 above that the frequency response does not differ significantly from the situation simulated without the presence of storage.

- Bus voltage

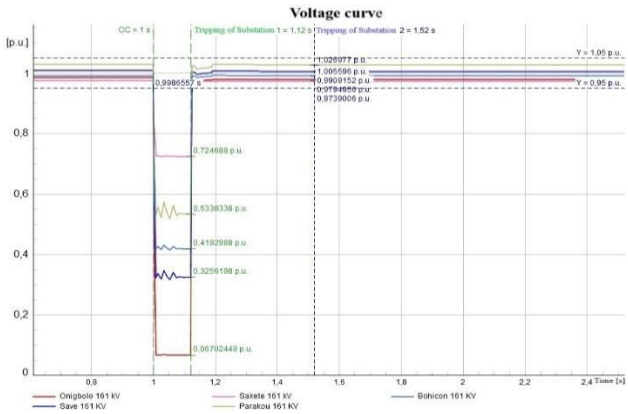


Figure-45. Voltage evolution at the nodes.

Figure-45 above shows the evolution of voltages at the different nodes of the network. These different curves remain within the acceptable range and behave in the same way as in the previous case without storage devices.

Moreover, it is useful to have an overview of the parameters of the 20 kV node.

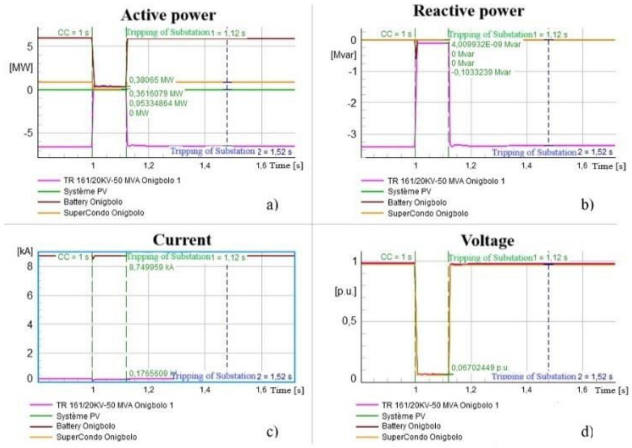


Figure-46. Parameters at the 20 kV node.

The curves in Figure-46 above present the network parameters at the 20 kV node of the Onigbolo substation, namely: active power, reactive power, current, and voltage.

The analysis of these curves reflects a typical behavior at this node following the applied short circuit.

- Loss of the Onigbolo-Bohicon line (fault at 1 second on the Onigbolo side at 2:30 PM)

- Contribution of the power plants

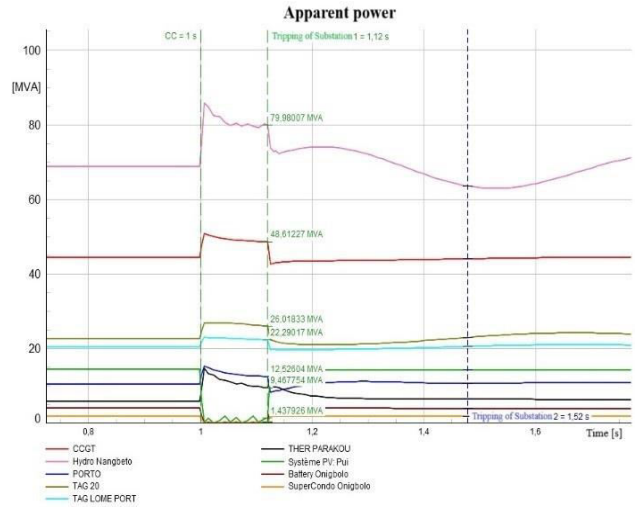


Figure-47. Apparent power.

Figure-47 illustrates the dynamic response of the grid in terms of apparent power following the short circuit

©2006-2026 Asian Research Publishing Network (ARPN). All rights reserved.

applied on the Onigbolo-Bohicon line at 2:30 PM (Onigbolo side), a period when solar production is active and storage devices are being recharged. It is also observed that the curves of the storage devices dropped to a value close to zero at the moment of the short circuit and stabilized after 1.12 seconds. The curves of all the machines are similar to those of the simulated fault case at the same time without storage devices or PV production, with negligible deviations.

- Contribution of the lines

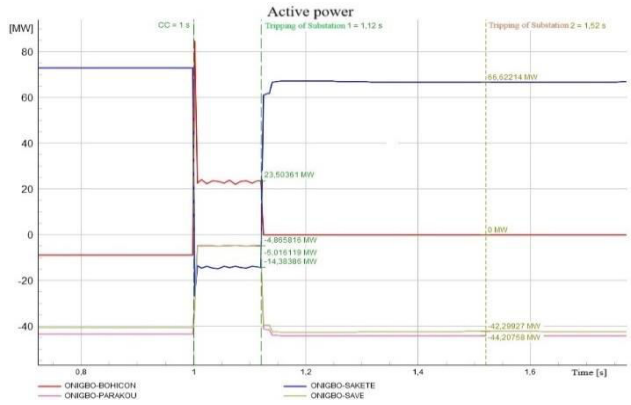


Figure-48. Active power of the lines.

The curves of the active powers transited, as shown in the graph of Figure-48 above, follow a pattern similar to that obtained for the scenario of the simulated fault in the absence of the PV production plant, the battery, and the supercapacitor.

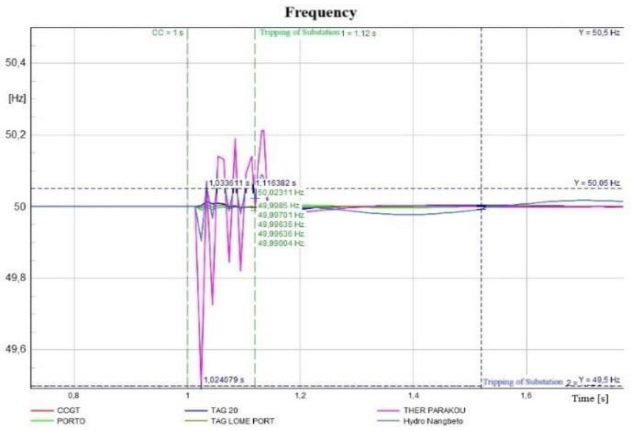


Figure-49. Frequency of groups.

The frequency curves, as shown in Figure-49 above, fluctuate as in the initial case before stabilizing from 1.12 s, a time after which the observed frequency values also comply with the permissible limits.

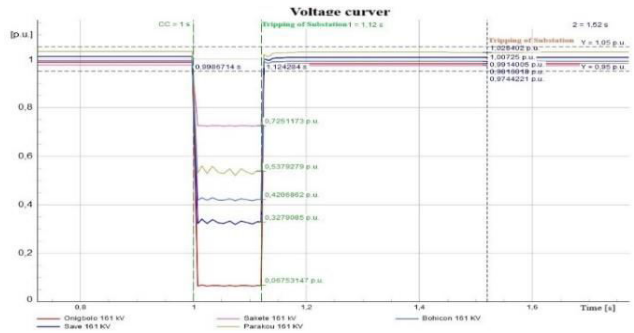


Figure-50. Voltage evolution at the nodes.

Figure-50 above also shows similar trends, to those of the case studied without PV or storage, for the voltage curves at the different nodes of the network during the short circuit. These curves stabilize from 1.12 seconds after the short circuit, while remaining within normal limits.

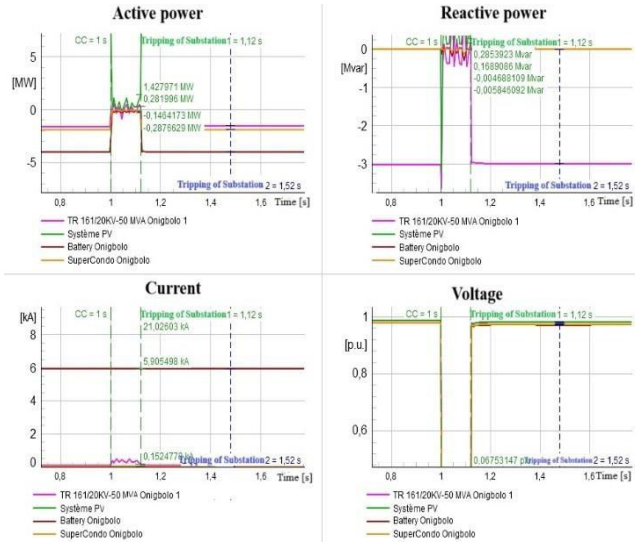


Figure-51. Parameters at the 20 kV node.

The graph in Figure-51 above presents, for the case of a simulated short circuit at 2:30 PM in the presence of PV and storage, the network parameters at the 20 kV node of the Onigbolo substation, namely: active power, reactive power, current, and voltage. The analysis of these curves reflects a typical behavior at this node following the applied short circuit.

©2006-2026 Asian Research Publishing Network (ARPN). All rights reserved.

Table-7. Compares key indicators across the three scenarios.

Indicators	Without éStorage	With Battery Only	Battery + Supercapacitor
Imported Energy	High (full dependence on the grid)	Reduced (optimized by battery)	Minimal (optimized peak management)
Self-consumption Rate	Low (no PV surplus storage)	Improved (partial PV storage)	Maximized (complementarity of systems)
Min/Max Voltage (p.u.)	0.95 – 1.05	0.96 – 1.05	0.95 – 1.05
Total Cost	High (high import costs)	Moderate (reduced imports)	Optimal (savings despite investment)
Average SOC (battery)	Not applicable	~70%	~75% (better cycle management)

4. STUDY LIMITATIONS

Although this study proposes innovative solutions for the integration of renewable energies, certain methodological simplifications limit their practical transposability. First, the assumption of a constant temperature neglects the impact of thermal variations on the performance of batteries (reduced efficiency outside of 15-40°C) and supercapacitors, potentially overestimating their durability and profitability in extreme climates.

Secondly, the fixed efficiency of inverters ignores energy losses outside the nominal range, underestimating operational costs and actual voltages.

Finally, the absence of modeling the aging of supercapacitors (20% capacity loss after 10^5 cycles) overestimates their long-term contribution to power peaks. If these limitations do not affect the central conclusions (grid stability, reduction of imports), they call for more realistic models for deployments under variable conditions or life cycle analyses.

5. CONCLUSIONS

This study demonstrates the technical and economic feasibility of a hybrid system integrating a 25 MWc PV plant, lithium-ion batteries (13.5 MWh), and 1MWh supercapacitors, thanks to an innovative methodology combining Simulink, PowerFactory, and the NSGA-II algorithm. The NSGA-II multi-objective optimization allowed for the definition of an optimal sizing, reconciling reduced costs (14.1 million XOF) and technical constraints (minimum SOC of 30%, maximum power of 20 MW for the supercapacitors).

The results obtained confirm the system's effectiveness: a reduction of 64.4 GWh/year in imports (-22%), a self-consumption rate of 78%, and robust network stabilization (voltages within 0.95-1.05 p.u., $\Delta f < 0.5$ Hz).

The simulations conducted in PowerFactory highlight the rapid response (< 1 second) to demand peaks of 12.5 MW and disturbances (short circuits), ensuring stable power supply. The validation at the DEFISOL site strengthens the credibility of the models, with efficient cyclic battery management and express recharging of the supercapacitors.

In summary, this work illustrates how the integration of hybrid storage (batteries and supercapacitors) optimized by advanced simulation and optimization tools allows for a balance between energy performance, grid stability, and profitability. The results, aligned with international standards (IEC/IEEE) and validated under real conditions, offer a reproducible model for resilient electrical grids, particularly in regions where the energy transition and access to reliable electricity are priorities. A review we recently conducted on PV-wind-fuel cell-battery hybrid architectures also highlighted the growing interest in multi-source systems for stationary applications, reinforcing the relevance of the hybridization approaches studied here [19]. This approach represents a significant advancement towards sustainable energy systems, capable of addressing the technical and economic challenges of modern networks.

6. EXTENSION PERSPECTIVES

This study opens promising technological avenues, including the integration of hydrogen storage for the long term, the replacement of Li-ion batteries with $LiFePO_4$ (safer and more resistant to extreme climates), and the use of AI to optimize weather forecasts and charging cycles. An in-depth analysis of the accelerated aging of components (batteries, supercapacitors) under real-world conditions (temperature, humidity) would allow for refining their lifespan and reliability.

REFERENCES

[1] 2025. Renewable Energy Sources and Climate Change Mitigation: Special Report of ... - Google Books. Consulted on: April 7, [Online].

©2006-2026 Asian Research Publishing Network (ARPN). All rights reserved.

[2] M. M. Gulzar, A. Iqbal, D. Sibtain and M. Khalid. 2023. An Innovative Converter less Solar PV Control Strategy for a Grid Connected Hybrid PV/Wind/Fuel-Cell System Coupled with Battery Energy Storage. IEEE Access, 11: 23245 23259.

[3] Kalogirou S. A. Artificial intelligence techniques for photovoltaic applications: a review. Prog. Energy Combust. Sci. 34, 547-632 | Request PDF.

[4] M. W. Leslie De, P. K. Chetangny, V. Zogbochi, M. Agbomahena, G. Barbier and D. Chamagne. 2024. Development of a Method for Estimating Solar and Wind Potential Based on Data Analysis, in 2024 IEEE PES/IAS Power Africa. pp. 1-5.

[5] M. G. Molina. 2017. Energy Storage and Power Electronics Technologies: A Strong Combination to Empower the Transformation to the Smart Grid, Proc. IEEE, 105(11): 2191 2219.

[6] A. Omar, M. Saghafifar, K. Mohammadi, A. Alashkar and M. Gadalla. 2019. A review of unconventional bottoming cycles for waste heat recovery: Part II - Applications, Energy Convers. Manag. 180: 559 583.

[7] L. H. Saw, Y. Ye and A. A. O. Tay. 2014. Electro-thermal analysis and integration issues of lithium-ion battery for electric vehicles, Appl. Energy. 131: 97 107.

[8] 2025. (PDF) A review of hybrid energy storage systems in renewable energy applications. Consulted on: April 7.

[9] A. Ibrahim. 2012. Renewable energy sources in the Egyptian electricity market: A review, Renew. Sustain. Energy Rev. 16(1): 216-230.

[10] W. Jing, C. Hung Lai, S. H. W. Wong and M. L. D. Wong. 2017. Battery-supercapacitor hybrid energy storage system in standalone DC microgrids: a review, IET Renew. Power Gener. 11(4): 461 469.

[11] R. Sebastián and R. Peña-Alzola. 2015. Control and simulation of a flywheel energy storage for a wind diesel power system, Int. J. Electr. Power Energy Syst. 64: 1049 1056.

[12] 2019. Thesis A HOUNNOU Amededjihunde-Hypolite-Jordao | PDF | Photovoltaic Solar Energy | Energy Storage.

[13] (PDF) Optimal Sizing of Hybrid Energy Systems in a Microgrid: A Review.

[14] J. Rocabert, A. Luna, F. Blaabjerg and P. Rodríguez. 2012. Control of Power Converters in AC Microgrids, IEEE Trans. Power Electron. 27(11): 4734-4749.

[15] K. Deb, A. Pratap, S. Agarwal and T. Meyarivan. 2002. A fast and elitist multiobjective genetic algorithm: NSGA-II, IEEE Trans. Evol. Comput. 6(2): 182-197.

[16] P. K. Chetangny *et al*. 2023. Optimization of a Diesel System - Stockpiling for Supplying a Remote BTS Station, in 2023 IEEE AFRICON. pp. 1-5.

[17] V. Lo Brano, A. Orioli, G. Ciulla and A. Di Gangi. 2010. An improved five-parameter model for photovoltaic modules, Sol. Energy Mater. Sol. Cells. 94(8): 1358 1370.

[18] P. K. Chetangny *et al*. 2023. Impact of ONIGBOLO's 25 MWp PV2 Solar Power Plant Connection on the Stability of Benin Transmission Grid, in 2023 IEEE AFRICON. pp. 1-6.

[19] P. K. Chetangny *et al*. 2023. Review of the Solar Photovoltaic - Wind - Fuel Cell - Battery Hybrid System for Stationary Applications, in 2023 International Conference on Electrical, Computer and Energy Technologies (ICECET). pp. 1-6.